

DIN-2025-0124

NONLINEAR DYNAMICS PERSPECTIVE FRAMEWORK EMPLOYED TO THE ANALYSIS OF ENERGY HARVESTERS

Luã Guedes Costa

Marcelo A. Savi

Universidade Federal do Rio de Janeiro, COPPE - Mechanical Engineering, Center for Nonlinear Mechanics, 21941-914 - Rio de Janeiro - RJ - Brazil

guedes@mecanica.coppe.ufrj.br, savi@mecanica.coppe.ufrj.br

Abstract. Since the 1990s, mechanical energy harvesting smart structures have been developed to power low-power electronic devices. The wide variety of proposed designs has made their characterization and comparison increasingly challenging. This work presents and emphasizes the authors' recent contributions to analyzing energy harvesting devices using a nonlinear dynamics perspective framework (NDPF). For that, four structures are examined, including two recently proposed designs by the authors and two classical devices established in the literature. The NDPF tools effectively map the dynamic and performance characteristics of these harvesters, allowing for a comprehensive comparison between its counterparts. Results demonstrate that NDPF analysis provides a robust solution for proper and accurate characterization of energy harvesting devices.

Keywords: Energy Harvesting, Nonlinear Dynamics, Computational Tools, Smart Structures, Analysis Framework

1. INTRODUCTION

The advancement of semiconductor technology has significantly reduced the energy needed to power electronic devices, especially IoT devices, standalone sensors, and MEMS. As a result, harvesting energy from mechanical sources has become an appealing solution, providing sufficient power for these innovations (duToit *et al.*, 2005).

Mechanical energy from the environment can be converted into electrical energy through various transduction mechanisms. Key methods include electromagnetic transducers, triboelectric phenomena, and smart materials like piezoelectric and magnetostrictive materials. Electromagnetic transducers work via electromagnetic induction, where changes in a magnetic field near a conductor induce a proportional electric current (Faraday, 1832). Triboelectric transducers leverage the triboelectric effect, generating electric charges through contact and friction between different materials (Liu *et al.*, 2021). Piezoelectric energy harvesting relies on the direct piezoelectric effect, where mechanical deformation of the material produces a corresponding electrical voltage (ANSI/IEEE, 1987). Magnetostrictive harvesting utilizes the Villari effect, where applying stress to a magnetostrictive material in a magnetic field alters its magnetization, which can be combined with electromagnetic induction for energy harvesting (Apicella *et al.*, 2019). These transducers are typically integrated into a primary structure, often a resonating cantilever beam, to maximize energy harvesting. However, cantilever-based designs suffer from performance drops when operating outside their narrow resonance range (Erturk and Inman, 2009).

One strategy to improve performance is incorporating nonlinear modulations. Common nonlinear systems, such as multistable systems induced by magnetic interactions or buckling forces, have been shown to enhance both bandwidth and power output (De Paula *et al.*, 2015). Nonsmooth systems also increase operational bandwidth, though at the cost of reduced maximum power (Ai *et al.*, 2019). Other structures, such as those using pendula, shape memory materials, rotational dynamics, asymmetry, and fluid-structure interactions, further improve performance (Zou *et al.*, 2019). Another approach is adding extra degrees of freedom to cantilever devices, creating additional high-performance regions due to new resonance zones (Wu *et al.*, 2013).

A review of the literature reveals a lot of proposed solutions in energy harvesting systems and a lack of standardized methods for analyzing and, more importantly, comparing nonlinear energy harvesters. This issue is compounded by potentially biased analyses that often highlight only the favorable attributes of the devices, making meaningful comparisons with similar systems difficult. For this reason, the authors recently proposed a framework of analysis based on a nonlinear dynamics perspective that allows proper characterization and comparison among harvesters (Costa *et al.*, 2021; Costa and Savi, 2024; Costa *et al.*, 2024). This work summarizes and this framework highlighting its main tools and demonstrating its application in two sets of distinct harvesters.

2. NDPF TOOLS

By examining the current literature, it became clear the lack of standardized methods for analyzing and, more critically, comparing nonlinear energy harvesters. The prevalent presence of potentially misleading analyses, which tend to showcase only the favorable attributes of the studied harvester, further increases the challenge of conducting meaningful comparisons with analogous devices. In response to these concerns, an analysis based on a nonlinear dynamics perspective was utilized by the authors in previous works. This section comprehensively summarizes the main set of tools that compose this integrated framework. This approach is designed to facilitate in-depth analyses of mechanical energy harvesters and enable proper comparisons among different configurations. By doing so, it is possible to concurrently investigate different (positive and negative) facets of the configurations proposed in this work. A brief description of the main framework techniques is elucidated in the next subsections.

2.1 Dynamical Responses Diagrams (DRDs)

Dynamical Responses Diagrams (DRDs) can be used as a tool to map and quantify the dynamical attractors of the system resulting from a specific initial condition within a 2D parameter space of choice. The diagrams are built with a grid of $N_x \times N_y$ sample points, each of which is obtained from a time series integration from an initial time, t_0 , to a final time, t_f , considering a suitable integration time step. A time t_{trans} is chosen to determine when in the time series the transient regime is considered to be over (usually it is chosen as $t_{\text{trans}} > 0.7t_f$). Additionally, all the samples have the same initial conditions to standardize the analysis.

From each sample, a behavior is classified. All classifications are based on the Lyapunov exponents spectrum and the verification of the steady state Poincaré map. Initially, the first two Lyapunov exponents, λ_1 and λ_2 , are analyzed. The

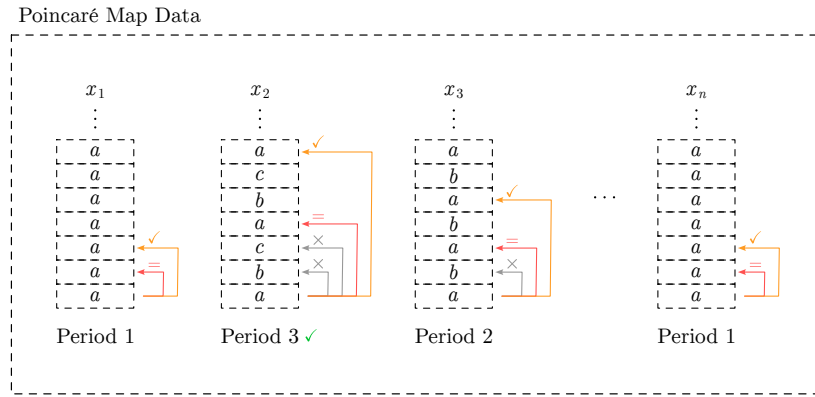


Figure 1. Procedure for classifying periodic attractors. a , b , and c represent real data, and x_1, x_2, \dots, x_n the state variables. Light gray arrows with “ \times ” indicate inequality, red arrows labeled “ $=$ ” show equality at the i^{th} position, and orange arrows with a \checkmark highlight when the $2i^{\text{th}}$ value equals the i^{th} . The largest classification is selected as the final classification, marked by a green checkmark.

behavior is classified based on the signal of the exponents, in which three behaviors are analyzed (periodic, chaotic and hyperchaotic). If the classification is chaotic or hyperchaotic, the classification procedure is over. Alternatively, if the classification is periodic, then the Poincaré map of the steady state time series sample is analyzed. A list of values with all the points of the Poincaré map is loaded, and the last point is used as the reference. Then, the previous points are analyzed one by one until it is found an equal at the i^{th} position. After that, if it finds another equal value in the $2i^{\text{th}}$ position, then it can be classified as a i -periodic candidate, if not, it continues to analyze previous points until these two conditions are met. The same procedure is done for all dimensions of the system, and the greatest periodic behavior found is used as the final classification. The comparison for all state variables is needed as limiting the observation to only one direction may yield misleading results of smaller periodicity due to the alignment of points in this direction. To avoid numerical errors, a tolerance of $p_{\text{tol}} = (x_{\max} - x_{\min})\mathcal{O}_{\text{method}}$ for each state variable must be placed when comparing the points, where x_{\max} and x_{\min} are the maximum and minimum values of the state variable between t_{trans} and t_f (steady state), and $\mathcal{O}_{\text{method}}$ is the order of error of the method of integration. The procedure depicting the comparison of the Poincaré map data is illustrated in Figure 1.

The resulting DRD is a 2-dimensional diagram where the different dynamical behaviors are classified by colors. In the context of this work, considering that T represents the excitation per period, the following classifications are considered: dark gray (1T), yellow (2T), green (3T), orange (4T) and purple (5T). Light blue is employed to represent responses with a period equal or greater than 6T, which means multiple periods (MP). Red regions represent chaotic (CH) responses, while dark red regions represent hyperchaotic (HC) responses.

2.2 Output Power Diagrams (OPDs) and Performance Comparison Diagrams (PCDs)

One-dimensional diagrams, typically frequency diagrams, are frequently used in the literature to analyze the performance of energy harvesting systems (Yuan *et al.*, 2019; Li *et al.*, 2021; Lan *et al.*, 2018). While this method has its merits, with the growing number of proposed harvesters, each with its own unique features and increasing complexity, this simplistic approach is proving to be inadequate. This approach often restricts the scope of analysis to a limited number of scenarios. Typically, the authors vary one of all key parameters (usually the amplitude or frequency of excitation) while keeping another key parameter constant. Also, they only consider a small set of values for that constant parameter. This practice can result in misleading conclusions as the entire excitation parameter space is not well evaluated. This limitation is particularly evident when comparing devices. Moreover, as computational power continues to increase, the generation, acquisition, and manipulation of larger datasets are becoming more feasible, even for entry-level personal computers. Consequently, the depth and sophistication of energy harvesting analysis, for both numerical and experimental analyses, must progress to align with these technological advancements.

In this work, the performance of the energy harvesters is evaluated in terms of a wider perspective, contemplating a considerable region of a parameter space of choice and summarizing the results in an Output Power Diagram (OPD). The construction of each OPD relies on a similar procedure of the construction of the DRDs. However, instead of evaluating the attractors, the OPDs show the steady state average electrical output power (or any variable related to that) under excitation conditions. This type of two-dimensional performance diagram is not new to the literature, it has been shown with other names in other works such as (Liao and Liang, 2019; Leadenham and Erturk, 2020). However, their application in a comparative scenario is new.

In this context, a comprehensive performance evaluation of two harvester configurations is conducted using a Performance Comparison Diagram (PCD). Each point on their OPDs is compared using a percentage difference metric, denoted as $\Delta P(\%)$, as outlined in Equation 1. Here, P_r represents the performance metric of the reference harvester, while P_s denotes the performance metric of the harvester under study.

$$\Delta P(\%) = [(P_s - P_r) / P_r] \times 100. \quad (1)$$

Equation 1 is used to compute the percentage difference, which allows a classification based on three sets:

- $\Delta P(\%) > 0$: The harvester under study shows better performance;
- $\Delta P(\%) = 0$: Both harvesters present the same performance;
- $\Delta P(\%) < 0$: The harvester used as reference shows better performance.

With these integrated tools, it is possible to map and quantify the performance of energy harvesters across a wide range of excitation conditions. Additionally, they enable robust comparisons between different energy harvester configurations.

2.3 Occurrence Diagrams (OCDs)

In general, nonlinear systems are characterized by their inherent complexity, where a small change in a parameter can lead to very different results, rendering the analysis of these systems a non-trivial task. To address that, it becomes advan-

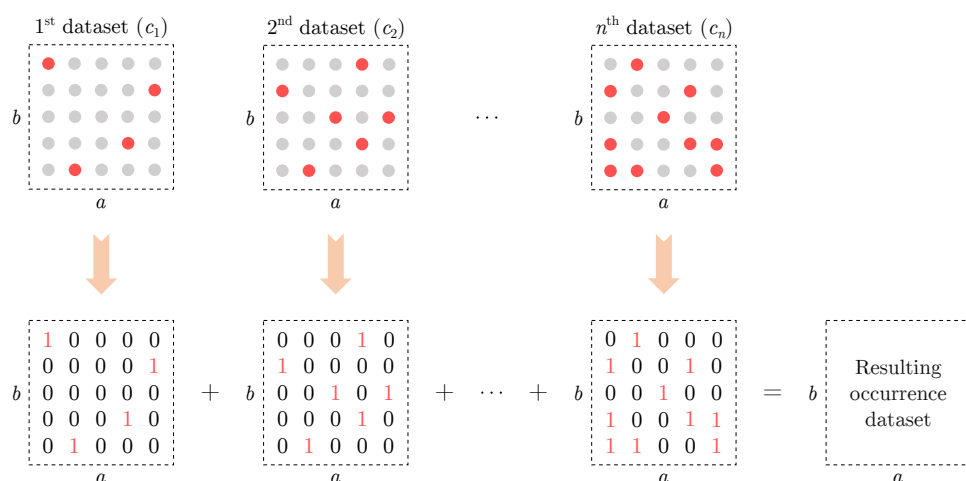


Figure 2. Procedure for constructing occurrence diagrams (OCDs). Red points indicate the desired characteristic, gray points do not. All red points are marked as 1 and gray points as 0. The final OCD is the sum of all datasets.

tageous to map specific characteristics within a parameter domain for a range of values of system parameters and evaluate the occurrence of that characteristic in each region of the parameter domain. The result of the analysis is summarized in an Occurrence Diagram (OCD), allowing for a more informed estimation of the likelihood of these target features emerging.

The procedure to construct an OCD involves the progressive analysis of different 2D diagram datasets. To illustrate this concept, consider a generic system characterized by three parameters: a , b and c . Within the parameter domain defined by $a \times b$, n distinct diagrams are generated, each representing a different value of the c parameter (c_1, c_2, \dots, c_n). Suppose our goal is to visually depict the prevalence of the *red characteristic* of the system and assess where, within the $a \times b$ parameter domain, this characteristic is most prominent for a range of values of c .

To accomplish this, the process begins by assigning the number 1 to all data points exhibiting the red characteristic and the number 0 to those that do not. Summing the values of each point in their respective locations within the parameter domain results in a dataset that reflects how frequently the red feature appears at each unique point in the domain. This procedure is illustrated in Figure 2.

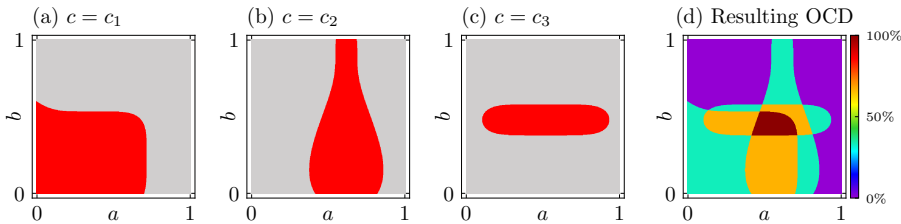


Figure 3. The first 3 columns show pseudo-random diagrams used to create the OCD in the 4th row. The colorbar indicates the likelihood of the red characteristic appearing in the $a \times b$ parameter space, based on the input diagrams.

Moreover, 3 pseudo-random data were generated to simulate a data collection, to provide a comprehensive view of how the number of analyzed sample diagrams influences the resulting OCD. In Figures 3a, 3b and 3c, these data collections are displayed in diagrams, which are used to construct the OCD. The resulting OCD, presented in Figure 3d, indicates that the area within the parameter space $a \times b$ that the red characteristic is mostly likely to emerge is predominantly centered at the intersection of the three red areas. This serves as a comprehensive illustration of the procedure outlined in Figure 2. Increasing the number of data available to construct the OCD provides more accuracy in the predictions.

When the construction of an OCD involves evaluating characteristics that can vary in maximum and minimum values across different sample diagrams, such as performance metrics in the context of energy harvesting, a normalization step must be performed before the summation of each dataset. This normalization takes the form of Equation 2, where $\bar{P}_{\text{norm},ij}$ is the normalized value of average output power, \bar{P}_{ij} , at each point in the single sample diagram, while $\bar{P}^{(\max)}$ denotes the maximum value of this characteristic across all points within the same diagram.

$$\bar{P}_{\text{norm},ij} = \bar{P}_{ij}/\bar{P}^{(\max)}, \quad (i = 1, \dots, N_x); (j = 1, \dots, N_y) \quad (2)$$

This normalization procedure results in all values within the sample diagrams being scaled to the range [0, 1], providing a measure of the quality of the characteristic.

In the next sections the NDPF is employed to analyze two distinct sets of energy harvesters: The first concerning multidirectional harvesters, while the second concerning multistable harvesters. Each set contains two harvesters with similar features, facilitating direct comparison. The models are dimensionless mathematical systems that capture the key qualitative characteristics of the harvesters, providing an overview of their physical attributes and performance. The parameters related to each harvester is summarized in Tab. 1.

3. MULTIDIRECTIONAL HARVESTERS

The classical piezoelectric energy harvester (CPEH) consists of a cantilever beam with a piezoelectric transducer near the fixed end and a tip mass at the free end. The multidirectional hybrid energy harvester (MHEH) builds on the CPEH by adding a pendulum at the free end, which provides multidirectional capabilities. An electromagnetic transducer is mounted at the pendulum's support to capture its rotational energy, enhancing performance.

The MHEH is described by the dimensionless equations in Eqs. (3) to (7). Equations (3) and (4) describe the motion of the harvester parallel and perpendicular to the beam's wider surface, respectively. Equation (5) details the pendulum's

Table 1. Simulation parameters for the energy harvesters.

Parameter	CBEH vs CMEH		CPEH vs MHEH		
	CBEH Value	CMEH Value	Parameter	CPEH Value	MHEH Value
Ω	0.01 → 10	0.01 → 10	Ω	0.01 → 2	0.01 → 2
γ	0.01 → 1	0.01 → 1	$\bar{\mu}$	45°	45°
ρ	0	1	ρ	0.5	0.5
ζ_1	0.025	0.025	ζ_x	0.025	0.025
ζ_2	0	0.025	ζ_z	0.025	0.025
Ω_s	0	0.25 → 2	ζ_ϕ	0	0.0025
α_1	-2	-2	Ω_s	1.87	0.01 → 2
α_2	0	-1	Ω_ϕ	0	0.05
β_1	1	1	ℓ	0	1
β_2	0	1	χ_{pz}	0.05	0.05
χ_1	0.05	0.05	χ_{em}	0	0.04
χ_2	0	0.05	κ_{pz}	0.5	0.5
κ_1	0.5	0.5	κ_{em}	0	0.4
κ_2	0	0.5	φ_{pz}	1	1
φ_1	0.05	0.05	φ_{em}	0	0.25
φ_2	0	0.05			

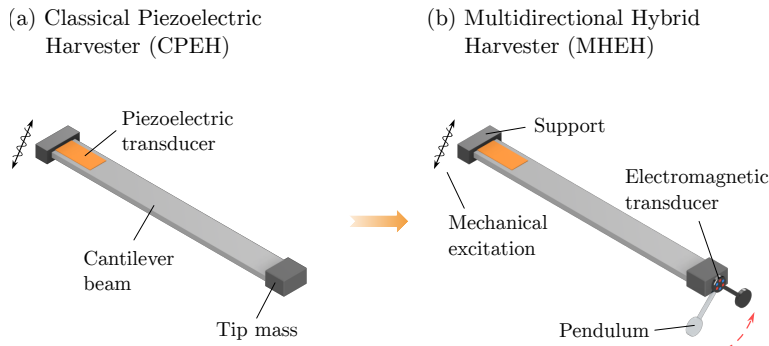


Figure 4. Conceptual representation of the evolution of the (a) classical piezoelectric energy harvester (CPEH) to (b) the multidirectional hybrid energy harvester (MHEH).

dynamics, while Eqs. (6) and (7) describe the dynamics of the piezoelectric and electromagnetic transducers.

$$(1 + \rho) \ddot{x} + 2\zeta_x \dot{x} + \Omega_s^2 \bar{x} + \rho \ell \left[\ddot{\phi} \cos(\bar{\phi}) - \dot{\phi}^2 \sin(\bar{\phi}) \right] = -(1 + \rho) \ddot{x}_b; \quad (3)$$

$$(1 + \rho) \ddot{z} + 2\zeta_z \dot{z} + \bar{z} - \chi_{pz} \bar{v} - \rho \ell \left[\ddot{\phi} \sin(\bar{\phi}) + \dot{\phi}^2 \cos(\bar{\phi}) \right] = -(1 + \rho) \ddot{z}_b; \quad (4)$$

$$\ddot{\phi} + 2\zeta_\phi \dot{\phi} + \Omega_\phi^2 \sin(\bar{\phi}) - \chi_{em} \bar{I} + \frac{1}{\ell} [\ddot{x} \cos(\bar{\phi}) - \ddot{z} \sin(\bar{\phi})] = \frac{1}{\ell} [\ddot{z}_b \sin(\bar{\phi}) - \ddot{x}_b \cos(\bar{\phi})]; \quad (5)$$

$$\dot{v} + \frac{\bar{v}}{\varphi_{pz}} + \kappa_{pz} \dot{z} = 0; \quad (6)$$

$$\dot{\bar{I}} + \varphi_{em} \bar{I} + \kappa_{em} \dot{\phi} = 0. \quad (7)$$

In this model, \bar{x} and \bar{z} are the generalized coordinates for the motions parallel and perpendicular to the larger surface of the beam, respectively, both relative to the base support. Subscripts \square_x and \square_z indicate variables associated with the x and z directions. The generalized coordinate $\bar{\phi}$ corresponds to the angular position of the pendulum, with the subscript \square_ϕ referring to variables related to the pendulum. Variables with subscripts \square_{pz} and \square_{em} are associated with the piezoelectric and electromagnetic transducers, respectively. The generalized coordinates \bar{v} and \bar{I} represent the voltage in the piezoelectric circuit and the electrical current in the electromagnetic circuit, respectively. The constant ζ is associated with the system's dissipation coefficients. Ω_s is the ratio between the x and z natural frequencies, while Ω_ϕ is the ratio between the pendulum's natural frequency and that of the z direction. The dimensionless constant ℓ relates to the pendulum's length, and ρ is the ratio between the equivalent masses of the pendulum and the beam. The parameters χ and κ are associated with the electromechanical coefficients of the transducers, while φ relates to the equivalent resistances of each transducer circuit. The multidirectional support excitation is defined by the harmonic functions $\bar{x}_b = \gamma \sin(\Omega\tau) \sin(\bar{\mu})$ and $\bar{z}_b = \gamma \sin(\Omega\tau) \cos(\bar{\mu})$, where γ and Ω are the excitation amplitude and frequency, respectively, and $\bar{\mu}$ is the angle of the excitation with respect to the perpendicular direction of the larger beam surface.

The CPEH is modeled by setting $\ell = \zeta_\phi = \Omega_\phi = \chi_{em} = \varphi_{em} = \kappa_{em} = 0$, while the MHEH includes all parameters as non-zero. The performance of each harvester is evaluated by computing the total average output power using the

following expressions:

$$\bar{P}_{\text{avg}}^{\text{CPEH}} = \frac{1}{\varphi_{pz}} (\bar{v}^{\text{RMS}})^2, \quad \bar{P}_{\text{avg}}^{\text{MHEH}} = \frac{1}{\varphi_{pz}} (\bar{v}^{\text{RMS}})^2 + \varphi_{em} (\bar{I}^{\text{RMS}})^2, \quad (8)$$

where the superscript $\square^{\text{RMS}} = \sqrt{\frac{1}{\tau_f - \tau_0} \int_{\tau_0}^{\tau_f} [\square(\tau)]^2 d\tau}$ refers to the root mean square (RMS) value of the generalized coordinate, where τ_0 and τ_f are the initial and final time of integration.

Consider the analysis of the MHEH. Using NDPF diagrams, a parametric analysis can be conducted to map and quantify the harvester's performance. Figure 5 provides an example of this mapping through 10 OPDs, which depict the average output power for varying excitation frequency values, Ω , across a two-dimensional parameter space defined by key structural parameters Ω_s and Ω_ϕ .

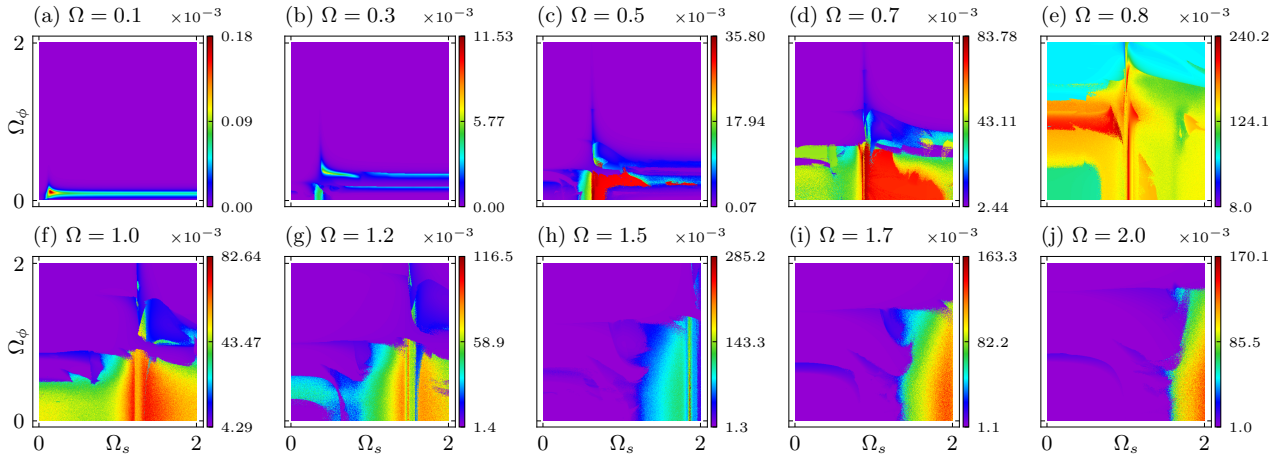


Figure 5. OPDs of \bar{P}_{avg} for a fixed excitation amplitude $\gamma = 0.3$, showing excitation frequencies from (a) $\Omega = 0.1$ to (t) $\Omega = 2$. Rainbow colorbars indicate the range of \bar{P}_{avg} values, with each diagram using 500×500 points.

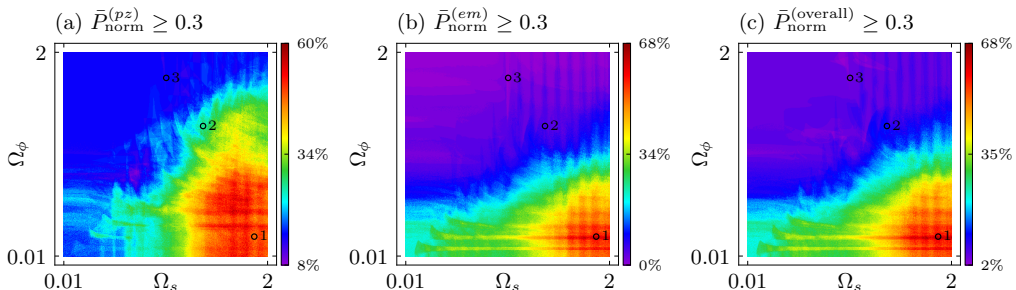


Figure 6. Occurrence Diagrams (OCDs) of the $\Omega_s \times \Omega_\phi$ parameter space for thresholds of (a) $\bar{P}_{\text{norm}}^{(pz)} \geq 0.3$, (b) $\bar{P}_{\text{norm}}^{(em)} \geq 0.3$, and (c) $\bar{P}_{\text{norm}}^{(\text{overall})} \geq 0.3$. Colorbars indicate the likelihood of each threshold, while black circles labeled 1-3 mark specific Ω_s and Ω_ϕ values of interest.

This mapping enables the determination of average output power for a broad set of key parameter values. By utilizing these data structures, an OCD can be generated to identify the optimal and suboptimal parameter combinations of Ω_s and Ω_ϕ . Figure 6 summarizes the results of this process using 100 different OPD datasets, applying a threshold value of $\bar{P}_{\text{norm}} = 0.3$ for all transducers. The OCDs reveal that lower values of Ω_ϕ paired with higher values of Ω_s favor higher performance, while the reverse leads to lower performance.

To further illustrate this, four points from the OCDs were selected, and the corresponding DRDs and OPDs for the excitation parameter domain, $\Omega \times \gamma$, are shown in Figure 7. In these cases, configuration 1 exhibit higher overall performance and a broader bandwidth, while configurations 3 and 4 demonstrate a gradual decline in performance. This reduction is primarily attributed to a drop in output power from the electromagnetic transducer, as indicated by the bar plots in the third column, which show the contribution of both piezoelectric (PZ) and electromagnetic (EM) components to total power.

Additionally, the dynamic and performance mapping allows for the association of both characteristics. Figure 8(a) shows the distribution of dynamical behaviors across all 100 cases, with 1T responses prevailing in 72% of instances. However, when focusing on cases where $\bar{P}_{\text{norm}} \geq 0.3$, hyperchaotic attractors dominate, indicating that most high-performance cases are linked to hyperchaotic dynamics.

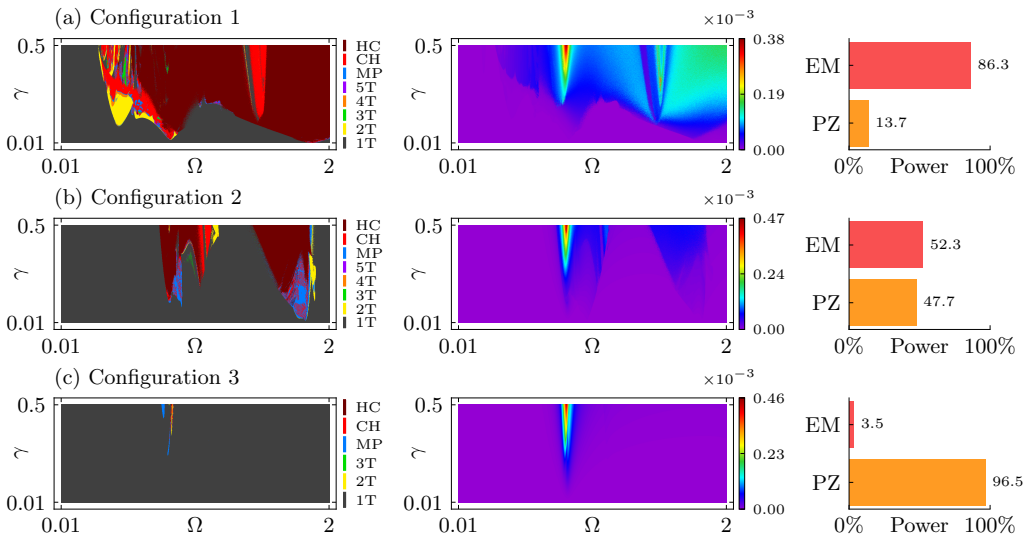


Figure 7. DRD, OPD for overall average output power \bar{P}_{avg} , and the power contribution of each transducer for (a) Config. 1, (b) Config. 2, and (c) Config. 3. DRD colorbars show different dynamical responses, while OPD colorbars display the range of \bar{P}_{avg} . Light red and orange bars represent the percentage contribution of the piezoelectric and electromagnetic transducers, respectively. Diagrams are based on a 1000×1000 grid in the $\gamma \times \Omega$ parameter space.

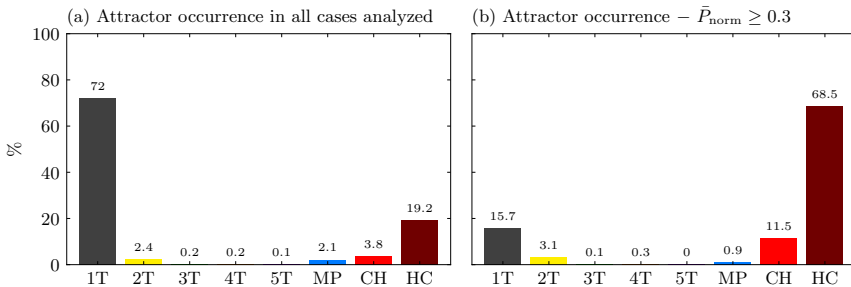


Figure 8. Percentage of dynamical responses for the 100 scenarios analyzed. (a) Overall percentage without filtering, (b) Attractors with $\bar{P}_{\text{norm}} \geq 0.3$ for both transducers, (c) Attractors with $\bar{P}_{\text{norm}}^{(pz)} \geq 0.3$.

Finally, Figure 9 presents the comparison results between the CPEH and the MHEH. Figures 9(a) and 9(b) display the OPDs for each harvester. The OPD for the CPEH highlights its narrow bandwidth, as documented in the literature. Incorporating a pendulum into the electromagnetic harvester significantly expands the operational bandwidth but reduces peak power, as shown by the OPD colorbars. The comparison is made using the PCD in Figure 9, which contrasts the performance of both harvesters. The results reveal that the CPEH only surpasses the MHEH within its resonance regions and a small adjacent area. In all other operational regions, the MHEH substantially outperforms the CPEH, as indicated by the red colorbar, truncated at 10000%.

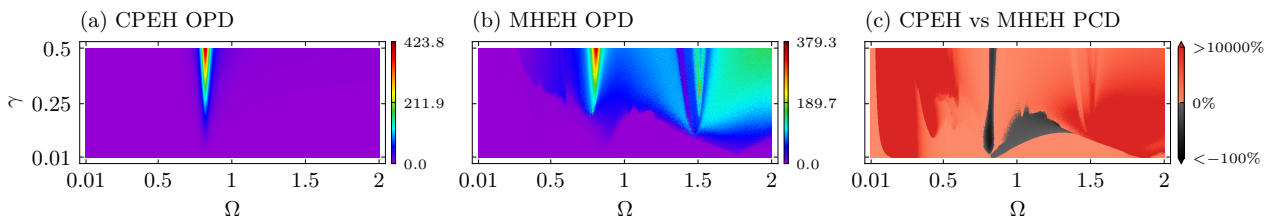


Figure 9. Comparison of harvesters: (a) OPD for CPEH, (b) OPD for MHEH, (c) PCD for CPEH vs MHEH. Rainbow colors in (a) and (b) denote \bar{P}_{avg} ; black and red in (c) indicate $\Delta \bar{P}(\%)$ per Eq. (1).

4. MULTISTABLE HARVESTERS

The conventional bistable energy harvester (CBEH) is composed of a cantilever beam working as a structural component. A piezoelectric patch is attached to the region near the beam's fixed end. A tip mass with a magnet is attached at the beam's free end. This magnet interacts with a fixed external magnet, and this interaction produces bistability. The

compact multistable energy harvester (CMEH) is a natural evolution of the bistable energy harvester as displayed in Fig. 10. In the CMEH, the main beam is modified to accommodate an inner beam with similar characteristics, resulting in a space-efficient design. This design places two transducers in previously unused space and introduces additional magnetic interactions, producing a compact harvester with multistable characteristics.

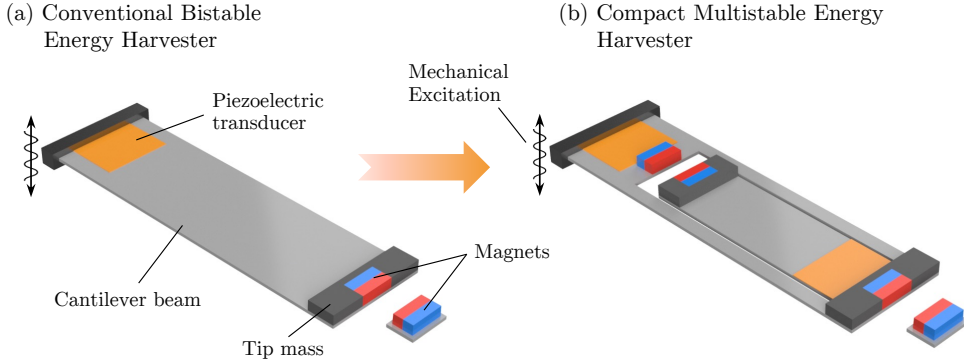


Figure 10. Conceptual representation of (b) the compact multistable energy harvester (CMEH), illustrating its compact and space-efficient design, which is comparable in size to (a) the conventional bistable energy harvester (CBEH).

The CMEH can be represented by the dimensionless system of Eqs. (9) to (12). Equation (9) describes the motion of the outer beam, while Eq. (10) describes the dynamics of the inner beam. Equations (11) and (12) are the expressions that represent the outer and inner piezoelectric elements, respectively.

$$\ddot{\bar{z}}_1 + 2\zeta_1 \dot{\bar{z}}_1 - 2\zeta_2 (\dot{\bar{z}}_2 - \dot{\bar{z}}_1) + (1 + \alpha_1) \bar{z}_1 + \beta_1 \bar{z}_1^3 - \rho \Omega_s^2 (\bar{z}_2 - \bar{z}_1) - \chi_1 \bar{v}_1 + \chi_2 \bar{v}_2 = -\ddot{\bar{z}}_b; \quad (9)$$

$$\rho \ddot{\bar{z}}_2 + 2\zeta_2 (\dot{\bar{z}}_2 - \dot{\bar{z}}_1) + \alpha_2 \bar{z}_2 + \beta_2 \bar{z}_2^3 + \rho \Omega_s^2 (\bar{z}_2 - \bar{z}_1) - \chi_2 \bar{v}_2 = -\ddot{\bar{z}}_b; \quad (10)$$

$$\dot{\bar{v}}_1 + \varphi_1 \bar{v}_1 + \kappa_1 \dot{\bar{z}}_1 = 0; \quad (11)$$

$$\dot{\bar{v}}_2 + \varphi_2 \bar{v}_2 + \kappa_2 (\dot{\bar{z}}_2 - \dot{\bar{z}}_1) = 0. \quad (12)$$

In this model, subscript \square_1 refers to the outer beam, while subscript \square_2 refers to the inner beam. The generalized coordinate \bar{z} represents the relative displacement perpendicular to the larger surface of the beam, and \bar{v} represents the voltage between the surfaces of each piezoelectric element. These generalized coordinates are functions of time, with $\dot{\square}$ denoting the time derivative. The mechanical dissipation coefficients are denoted by ζ . The polynomial coefficients α and β fit the total resulting nonlinear restitution force of the magnetic interactions. The ratio between the inner and outer equivalent masses is represented by ρ , and Ω_s is the ratio between the first natural frequencies of the inner and outer beams. The electromechanical couplings of the piezoelectric elements in the mechanical and electrical equations are denoted by χ and κ , respectively. The term φ is related to the inverse of the resistance in each piezoelectric equivalent circuit. Finally, $z_b = \gamma \sin(\Omega\tau)$ describes a harmonic support excitation, where γ is the amplitude, Ω is the frequency of excitation, and τ is time.

The CBEH can be described by making $\rho = \Omega_s = \zeta_2 = \alpha_2 = \beta_2 = \chi_2 = \varphi_2 = \kappa_2 = 0$, while the CMEH is represented by all parameters different from zero. The performance of each harvester can be done by evaluating the total average output power of each harvester utilizing the following expressions:

$$\bar{P}_{\text{avg}}^{\text{CBEH}} = \varphi_1 (\bar{v}_1^{\text{RMS}})^2, \quad \bar{P}_{\text{avg}}^{\text{CMEH}} = \sum_{i=1}^2 [\varphi_i (\bar{v}_i^{\text{RMS}})^2]. \quad (13)$$

Consider the analysis of the CMEH. Using NDPF diagrams, various configurations with different structural parameter values, Ω_s , can be examined, as shown in Fig. 11. Each column represents a distinct configuration: the first row displays the corresponding DRD, while the second row presents the corresponding OPD for each configuration. The results demonstrate that varying structural parameters shifts the peak power region toward higher frequencies, Ω , as changes in Ω_s alter the system's fundamental frequencies. However, the overall shape and characteristics of the performance distribution across the two-dimensional parameter domain remain largely consistent between configurations, with regions of high, medium, and low performance located similarly within the diagrams. The analysis presented in Figure 11 suggests the need for a more detailed investigation to identify the optimal performance regions. To this end, consider constructing an OCD with eight distinct OPDs corresponding to different configurations, each with a unique Ω_s value from the set $(0.25, 0.5, 0.75, 1.0, 1.25, 1.5, 1.75, 2.0)$, as shown in Figure 12(a) for $\bar{P}_{\text{norm}} \geq 0.01$. This threshold highlights regions where the harvester achieves more than 1% of the maximum \bar{P}_{avg} . Using this approach, areas of interest can be identified and delineated, as shown in Figure 12(b). The green area, labeled A, represents the region

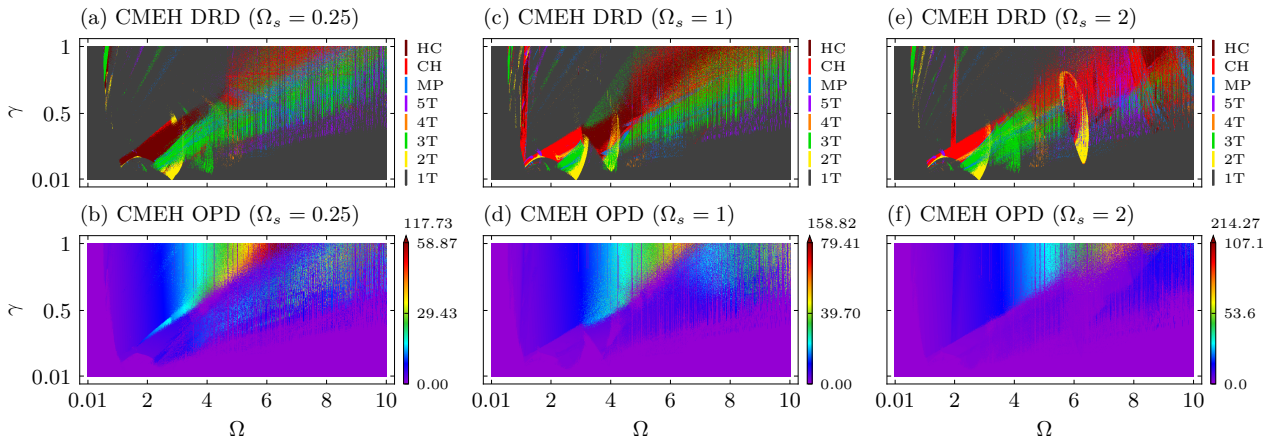


Figure 11. CMEH dynamics and performance mapping: (a) DRD for $\Omega_s = 0.25$, (b) OPD for $\Omega_s = 0.25$, (c) DRD for $\Omega_s = 1$, (d) OPD for $\Omega_s = 1$, (e) DRD for $\Omega_s = 2$, (f) OPD for $\Omega_s = 2$.

of highest performance, with a consistent concentration of good results. In contrast, the yellow area, labeled B, shows significant fluctuations due to intermittent irregular points of high and low performance. Region C, shown in orange, is similar to B but with fewer occurrences. Finally, the red area, labeled D, indicates poor performance and should be avoided in the harvester's design. Consequently, regions A, B, and C are classified as areas of interest.

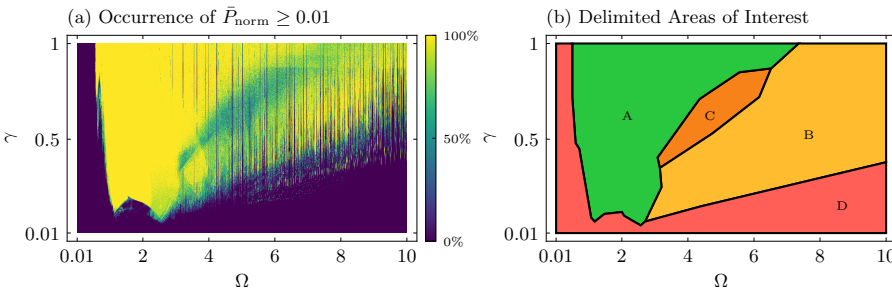


Figure 12. (a) OCD for $\bar{P}_{\text{norm}} \geq 0.01$. (b) Identified regions of interest

After identifying the regions of interest, a single CMEH configuration with $\Omega_s = 0.25$ is selected, and the comparison with the CBEH is displayed in Figure 13. Figure 13(a) presents the OPD for the CBEH, while Figure 13(b) illustrates the OPD for the CMEH. Figure 13(c) shows the PCD comparing both OPDs. Both harvesters display similar OPD patterns, with regions of low, medium, and high performance occurring in comparable areas of the two-dimensional parameter space. However, the CMEH achieves nearly twice the maximum performance of the CBEH, as reflected by the colorbars. The PCD in Figure 13(c) offers a clearer comparison, with the colorbar limits truncated by 50% for better visualization. In the medium to high performance regions, the PCD demonstrates that the CMEH consistently outperforms the CBEH.

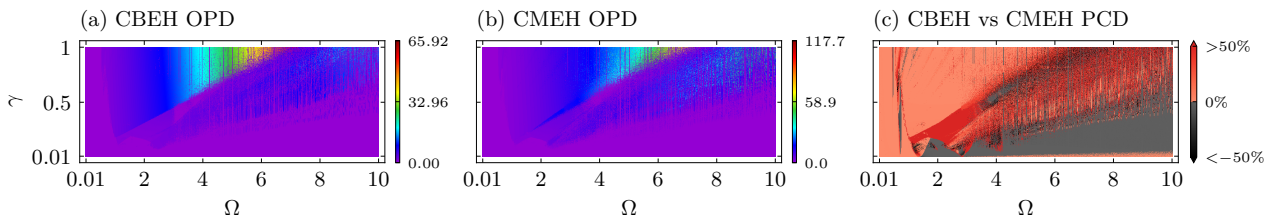


Figure 13. Comparison of harvesters: (a) OPD for CBEH, (b) OPD for CMEH, (c) PCD for CBEH vs CMEH. Rainbow colors in (a) and (b) denote \bar{P}_{avg} ; black and red in (c) indicate $\Delta\bar{P}(\%)$ per Eq. (1).

5. CONCLUSIONS

This work highlights the importance of a nonlinear dynamics approach for mapping, quantifying, and understanding the key design characteristics of energy harvesting systems. It summarizes and demonstrates the main tools from the recently proposed Nonlinear Dynamics Perspective Framework (NDPF) on two sets of energy harvesters: the first set includes two types of multistable harvesters, and the second set features a classical piezoelectric harvester and a multi-

directional hybrid harvester. The demonstrations effectively identify the optimal and suboptimal parameter combinations and provide a thorough comparison of the harvesters across a broad excitation parameter space.

The nonlinear dynamics approach enables a deeper exploration of the complex behaviors and interactions within these systems, leading to more efficient and robust designs. This approach is especially relevant today, with the widespread availability of high-performance computing. Moreover, these techniques are recommended for both numerical and experimental studies, as they are applicable to practical scenarios.

6. ACKNOWLEDGEMENTS

The authors would like to acknowledge the support of the Brazilian Research Agencies CNPq (Conselho Nacional de Desenvolvimento Científico e Tecnológico), CAPES (Coordenação de Aperfeiçoamento de Pessoal de Nível Superior) and FAPERJ (Fundação Carlos Chagas Filho de Amparo à Pesquisa do Estado do Rio de Janeiro) and through the INCT-EIE (National Institute of Science and Technology - Smart Structures in Engineering), CNPq, CAPES and FAPEMIG (Fundação de Amparo à Pesquisa do Estado de Minas Gerais). The support of the AFOSR (Air Force Office of Scientific Research) (FA9550-23-1-0527) is also acknowledged. Moreover, the authors also appreciate the use of the computational resources of the NACAD (Advanced High-Performance Computing Nucleus).

7. REFERENCES

- Ai, R., Monteiro, L.L.S., Monteiro, P.C.C., Pacheco, P.M.C.L. and Savi, M.A., 2019. "Piezoelectric vibration-based energy harvesting enhancement exploiting nonsmoothness". *Actuators*, Vol. 8, No. 1. doi:10.3390/act8010025.
- ANSI/IEEE, 1987. "Ieee standard on piezoelectricity (std 176)".
- Apicella, V., Clemente, C.S., Davino, D., Leone, D. and Visone, C., 2019. "Review of modeling and control of magnetostrictive actuators". *Actuators*, Vol. 8, No. 2. doi:10.3390/act8020045.
- Costa, L.G., Monteiro, L.L.S. and Savi, M.A., 2024. "Multistability investigation for improved performance in a compact nonlinear energy harvester". *Journal of the Brazilian Society of Mechanical Sciences and Engineering*, Vol. 46, No. 4, p. 212.
- Costa, L.G. and Savi, M.A., 2024. "Nonlinear dynamics of a compact and multistable mechanical energy harvester". *International Journal of Mechanical Sciences*, Vol. 262, p. 108731.
- Costa, L.G., da Silva Monteiro, L.L., Pacheco, P.M.C.L. and Savi, M.A., 2021. "A parametric analysis of the nonlinear dynamics of bistable vibration-based piezoelectric energy harvesters". *Journal of Intelligent Material Systems and Structures*, Vol. 32, No. 7, pp. 699–723.
- De Paula, A.S., Inman, D.J. and Savi, M.A., 2015. "Energy harvesting in a nonlinear piezomagnetoelastic beam subjected to random excitation". *Mechanical Systems and Signal Processing*, Vol. 54-55, pp. 405–416.
- duToit, N.E., Wardle, B.L. and Kim, S.G., 2005. "Design considerations for mems-scale piezoelectric mechanical vibration energy harvesters". *Integrated Ferroelectrics*, Vol. 71, No. 1, pp. 121–160.
- Erturk, A. and Inman, D.J., 2009. "An experimentally validated bimorph cantilever model for piezoelectric energy harvesting from base excitations". *Smart Materials and Structures*, Vol. 18, No. 2, p. 025009.
- Faraday, M., 1832. "V. experimental researches in electricity". *Philosophical Transactions of the Royal Society of London*, Vol. 122, pp. 125–162.
- Lan, C., Tang, L. and Harne, R.L., 2018. "Comparative methods to assess harmonic response of nonlinear piezoelectric energy harvesters interfaced with ac and dc circuits". *Journal of Sound and Vibration*, Vol. 421, pp. 61–78.
- Leadenham, S. and Erturk, A., 2020. "Mechanically and electrically nonlinear non-ideal piezoelectric energy harvesting framework with experimental validations". *Nonlinear Dynamics*, Vol. 99, No. 1, pp. 625–641. ISSN 1573-269X.
- Li, H., Sun, H., Song, B., Zhang, D., Shang, X. and Liu, D., 2021. "Nonlinear dynamic response of an l-shaped beam-mass piezoelectric energy harvester". *Journal of Sound and Vibration*, Vol. 499, p. 116004.
- Liao, Y. and Liang, J., 2019. "Unified modeling, analysis and comparison of piezoelectric vibration energy harvesters". *Mechanical Systems and Signal Processing*, Vol. 123, pp. 403–425.
- Liu, L., Guo, X., Liu, W. and Lee, C., 2021. "Recent progress in the energy harvesting technology—from self-powered sensors to self-sustained iot, and new applications". *Nanomaterials*, Vol. 11, No. 11. doi:10.3390/nano11112975.
- Wu, H., Tang, L., Yang, Y. and Soh, C.K., 2013. "A novel two-degrees-of-freedom piezoelectric energy harvester". *Journal of Intelligent Material Systems and Structures*, Vol. 24, No. 3, pp. 357–368.
- Yuan, T.C., Yang, J. and Chen, L.Q., 2019. "Nonlinear vibration analysis of a circular composite plate harvester via harmonic balance". *Acta Mechanica Sinica*, Vol. 35, No. 4, pp. 912–925. ISSN 1614-3116.
- Zou, H.X., Zhao, L.C., Gao, Q.H., Zuo, L., Liu, F.R., Tan, T., Wei, K.X. and Zhang, W.M., 2019. "Mechanical modulations for enhancing energy harvesting: Principles, methods and applications". *Applied Energy*, Vol. 255, p. 113871.

8. RESPONSIBILITY NOTICE

The authors are solely responsible for the printed material included in this paper.